Science of the Total Environment 955 (2024) 176838

Contents lists available at ScienceDirect

Science of the Total Environment

journal homepage: www.elsevier.com/locate/scitotenv

A mixed layer height parameterization in a 3-D chemical transport model: Implications for gas and aerosol simulations

Hyeonmin Kim [a], Rokjin J. Park [a,*], Song-you Hong [b,c], Do-Hyeon Park [d], Sang-Woo Kim [a], Yujin J. Oak [e], Xu Feng [e], Haipeng Lin [e], Tzung-May Fu [f,g]

[a] School of Earth and Environmental Sciences, Seoul National University, Seoul, South Korea
[b] Cooperative Institute for Research in Environmental Sciences, University of Colorado, Boulder, USA
[c] Physical Sciences Laboratory, the National Oceanic and Atmospheric Administration Earth System Research Laboratories, Boulder, USA
[d] Center for Sustainable Environment Research, Korea Institute of Science and Technology, Seoul, South Korea
[e] John A. Paulson School of Engineering and Applied Sciences, Harvard University, Cambridge, MA, USA
[f] State Environmental Protection Key Laboratory of Integrated Surface Water-Groundwater Pollution Control, School of Environmental Science and Engineering, Southern University of Science and Technology, Shenzhen, Guangdong, China
[g] Shenzhen Institute of Sustainable Development, Southern University of Science and Technology, Shenzhen, Guangdong, China

HIGHLIGHTS

- We introduce a novel MLH parameterization based on the YSU PBL scheme.
- Simulated MLH shows a better agreement with observed PBLH than the YSU PBL scheme.
- The model with MLH improves NO_X overestimations and O_3 underestimations.
- Using MLH alters the speed of N_2O_5 chemistry and vertical distributions of NH_3.
- These changes lead to better model performance in aerosol simulations.

GRAPHICAL ABSTRACT

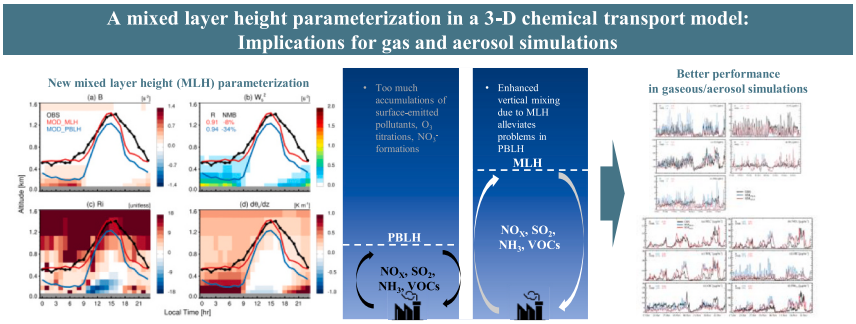

ARTICLE INFO

Editor: Alessandra De Marco

Keywords:
Planetary boundary layer
Mixed layer height
The SIJAQ campaign
WRF-GC
Aerosol chemistry
Particulate matter

ABSTRACT

Vertical mixing within the planetary boundary layer (PBL) is crucial for determining surface-level pollutant concentrations. However, standard PBL schemes in chemical transport models (CTMs) often fail to adequately define the upper bounds of vertical mixing, particularly at night. This limitation frequently results in overestimated nocturnal concentrations of pollutants near the surface. To address this issue, we propose a parameterization of mixed layer height (MLH) derived from the Yonsei University (YSU) PBL scheme and thoroughly evaluate it by comparing simulations with various observations. We utilized the Weather Research and Forecasting model coupled with GEOS-Chem (WRF-GC) to simulate gas and aerosol distributions over South Korea during the Satellite Integrated Joint Monitoring of Air Quality (SIJAQ) campaign in 2021. The WRF-GC simulations incorporating the MLH parameterization improved the excessive titration of O_3 and the overproduction of HNO_3 and NO_3^- in the model. Consequently, the model performances in gaseous and aerosol simulations showed a better agreement with observations, with changes in normalized mean biases (NMBs) of NO_X (from 50 % to

* Corresponding author.
E-mail address: rjpark@snu.ac.kr (R.J. Park).

https://doi.org/10.1016/j.scitotenv.2024.176838
Received 6 July 2024; Received in revised form 22 September 2024; Accepted 8 October 2024
Available online 11 October 2024

−27 %), O_3 (from −49 % to −28 %), NO_3^- (from 126 % to 91 %), NH_4^+ (from 113 % to 85 %), BC (from 322 % to 135 %), and $PM_{2.5}$ (from 58 % to 28 %).

1. Introduction

The planetary boundary layer (PBL) is the lowest part of the Earth's atmosphere, where energy, momentum, moisture, gases, and aerosols are exchanged between the Earth's surface and the free atmosphere (Gerbig et al., 2008; Stull, 1988). The PBL height (PBLH) marks the upper limit of the direct influence of the Earth's surface, inhibiting the vertical transport of surface-emitted pollutants to regions above the PBLH (Li et al., 2017). Thus, understanding the structure and diurnal evolution of PBLH is crucial for weather forecasting and pollution dispersion modeling.

Detecting PBLH has been a significant focus in atmospheric sciences for several decades, leading to the development of various estimation methods. A direct measurement of PBLH is impossible; instead, it is estimated indirectly through different observations. Radiosonde measurements are the primary method for detecting PBLH (Li et al., 2021; Liang and Liu, 2010). However, this technique faces challenges in providing comprehensive spatial and temporal coverage due to technical and economic limitations. Remote sensing techniques, such as lidar or satellite observations, can extend the spatiotemporal detection of PBLH, albeit with notable uncertainties (Kim et al., 2021; Park et al., 2022).

Numerical models have been employed to overcome the spatiotemporal limitations of observation-based PBLH detection (Bravo-Aranda et al., 2017; Hong et al., 2006). Various PBL schemes based on thermal and mechanical mixing have been proposed and implemented in weather forecasting and climate models, demonstrating reasonable performances compared to observations (Canuto et al., 2001; Rai and Pattnaik, 2019; Shin and Hong, 2011). The models' PBL schemes are crucial for transferring momentum, heat, and moisture between the surface and the atmosphere (Holtslag and Boville, 1993; Stull, 1988).

The PBL schemes are also essential for simulating the dispersion and fate of surface-emitted pollutants in Chemical Transport Models (CTM) (Jia and Zhang, 2020; Banks and Baldasano, 2016; Onwukwe and Jackson, 2020). However, preceding studies have reported that the conventional PBL schemes may not correctly represent the vertical mixing of pollutants in CTMs because they are highly overweighted on thermally induced convection and underestimate vertical mixing by mechanical forcing (Jordan et al., 2010; Lee et al., 2023; Oak et al., 2019; Travis et al., 2022).

This misrepresentation of PBL schemes in CTMs leads to significant uncertainties in the vertical distributions of pollutants (Shi et al., 2020). Indeed, significant overestimations in primary and secondary aerosols in CTM have been reported due to PBLH underestimation (Lee et al., 2023; Travis et al., 2022). Also, too much accumulation of simulated NO near the surface titrates O_3, causing overestimations in NO_X and underestimation in O_3 in the model (Oak et al., 2019; Travis et al., 2022). The issue with PBL representation leads to an imbalance in the exchange of trace gases between the PBL and the free troposphere, causing uncertainty in the model's vertical distribution of OH reactivity (Kim et al., 2022).

Here, we introduce a mixed layer height (MLH) parameterization based on the Yonsei University (YSU) PBL scheme to better represent the vertical mixing of trace gases and aerosols in CTMs. In micrometeorology studies, MLH is conventionally considered as a subset of PBLH. We here do not follow this conventional terminology. Our MLH parameterization aims to reproduce the lidar-detected boundary layer height based on observed vertical distributions of pollutants (Park et al., 2021a; Park et al., 2022). The MLH parameterization and its effect on gaseous and aerosol simulations are validated using observation-based PBLH data from lidar observations and observed gaseous and aerosol concentrations in South Korea during the Satellite Integrated Joint Monitoring of Air Quality (SIJAQ) campaign in 2021. For convenience hereafter, we refer to "lidar-detected boundary layer height" as "observed PBLH".

2. Observations

South Korea's National Institute of Environmental Research (NIER) conducted the SIJAQ campaign over the Korean peninsula from October to November 2021. The campaign provided an extensive observation dataset of gaseous and aerosol species at Olympic Park (127.13°E, 37.52°N, Fig. 1b), which is located in the middle of a green space surrounded by a high-density residential area and freeways in the Seoul Metropolitan Area (SMA).

Kim et al. (2023) categorized the campaign into five meteorological periods: sustained warm-stagnant (October 10–28, P1), stagnant high (October 29–November 7, P2), migratory low (November 8–14, P3), migratory high (November 15–21, P4), migratory low (November 22–25, P5). The P1 period was influenced by marine stagnation. The P2–P4 periods are a transition to continental influence. The P5 period was under continental influence. An increase in high $PM_{2.5}$ and PM_{10} concentrations was found in the P2 and P4 periods. Moderate PM concentrations are shown in the P1 period, but relatively clean air quality was found in the P3 and P5 periods.

During the campaign, ion chromatography (Dionex, Sunnyvale, CA, USA) measured NO_3^-, SO_4^{2-}, and NH_4^+ aerosol concentrations every four hours. Organic carbon (OC) and black carbon (BC) aerosol concentrations were analyzed using a thermal, optical transmittance carbon analyzer (Sunset model 5) following the NIOSH method 5040 (Birch and Cary, 1996) with a 4-h temporal resolution. The beta-ray method (Shin et al., 2011; Takahashi et al., 2008) was used to measure hourly particulate matter ($PM_{2.5}$) concentrations.

Gaseous species, including O_3, SO_2, and CO, were measured every 1 min with Ozone Analyzer 49iQ, Pulsed Fluorescence SO_2, Analyzer 43i, and Gas Filter Correlation CO Analyzer 48i (Thermo Fisher Scientific, USA), respectively. NO and NO_2 concentrations were observed every 1 min by chemiluminescence with a molybdenum converter (Marley et al., 2004) and Cavity Attenuated Phase Shift (CAPS) Trace-level NO_2 Analyzer.

The AirKorea monitoring network, managed by NIER and affiliated with the Korean Ministry of Environment (https://www.airkorea.or.kr/eng, accessed September 2, 2024), provided hourly measurements of volume mixing ratios of SO_2, CO, O_3, and NO_2 and mass concentrations of $PM_{2.5}$ over the stations at Seoul (Fig. 1b).

An elastic lidar located at Seoul National University (SNU, 126.95°E, 37.45°N, 116 m above sea level, Fig. 1b) measured the attenuated backscatter intensity (β) and depolarization ratio of the 532 nm laser signal at 15-min intervals, with a vertical resolution of 6 m on average (Pappalardo et al., 2014; Weitkamp, 2006). To ensure data reliability, measurements up to 120 m were excluded due to incomplete overlap issues, which may impact the retrieval of observed PBLH at lower altitudes (Park et al., 2022). Cloud detection was based on total attenuated backscatter values because clouds exhibit stronger signals than aerosols over narrower altitude ranges. We discarded observations with strong backscatter values ($\beta > 1.5 \times 10^{-5}$ m^{-1} sr^{-1} below 1 km and $> 10^{-5}$ m^{-1} sr^{-1} above 1 km) as cloud presence (Kim et al., 2015).

The observed PBLH was determined as the height at which a drastic decrease in lidar observed β values occurs, assuming a uniform distribution of aerosols within PBL (Kim et al., 2007). The lidar profile was examined in moving bundles of the 3-point (90 m) (the 3-point gradient method) to detect sharp decreases in β (Kim et al., 2015). A possible

deterioration by the nocturnal residual layer is prevented by adopting a threshold value for the vertical gradient of the range-corrected signal, as conducted by Park et al. (2021a). Detailed information about calculating PBL heights using lidar data and its evaluation against other independent observations can be found in Park et al. (2021a). All the observations used in this study and their related information are summarized in Table 1.

3. Model description

3.1. The YSU PBL scheme

The YSU PBL scheme is an adapted K-theory model, including countergradient terms to account for the influence of large-scale eddies on the total flux (Holtslag and Boville, 1993; Hong, 2010; Hong et al., 2006). For $z \leq$ PBLH, the turbulence diffusion of prognostic variables (C), including zonal wind u, meridional wind v, vertical wind w, potential temperature θ, specific humidity q, and air pollutant concentrations, is computed using Eq. (1) as follows:

$$\frac{\partial C}{\partial t} = \frac{\partial}{\partial z}\left\{K_C\left(\frac{\partial C}{\partial z} - \gamma_C\right) - \overline{(w'C')}_h\left(\frac{z}{h}\right)^3\right\} \quad (1)$$

, where K_C is the eddy diffusivity coefficient, γ_C is a correction to the local gradient to incorporate the contribution of the large-scale eddies to the total flux, and $\overline{(w'C')}_h$ is the flux at the inversion layer. z is the height of model levels, and h is PBLH. The detailed equations for calculating each term in the Eq. (1) can be found in Hong (2010).

PBLH, h, in the Eq. (1) is determined as the first model level from the surface, below which the averaged bulk Richardson number (Ri_b) from the surface is equal to or greater than the critical values (0.0 for unstable and 0.25 for stable conditions) (Hong, 2010). The Ri_b is calculated using the Eq. (2) below.

$$Ri_b(z) = \frac{g[\theta_v(z) - \theta_s]z}{\theta_{va}U(z)^2} \quad (2)$$

, where $U(z)$ is the horizontal wind speed at z, and $\theta_v(z)$ is the virtual potential temperature at z. g is gravitational acceleration. θ_{va} is the virtual potential temperature at the lowest model level. θ_s is a temperature calculated as follows:

$$\theta_s = \theta_{va} + \theta_T, where\ \theta_T = a\frac{\overline{(w'\theta_v')}_0}{w_{s0}} \quad (3)$$

, where the proportionality factor a is 6.8. The mixed layer velocity scale w_{s0} is the value at $z = 0.5\ h$, and the detailed expression for its calculation can be found in Hong (2010).

As will be discussed, however, the PBLH in the YSU PBL scheme is significantly shallower than the observed PBLH (Oak et al., 2019; Travis et al., 2022), especially during nighttime. We also find that this nighttime underestimation of PBLH is a general problem found in other schemes in WRF, including Mellor–Yamada–Janjic (MYJ) and

Table 1
Observations used in this study and related information.

Species	Instrument	Resolution	References
NO_3^-, SO_4^{2-}, NH_4^+	Ion chromatography	4-h	(Dionex, Sunnyvale, CA, USA)
BC, OC	A thermal, optical transmittance carbon analyzer (Sunset model 5) with the NIOSH method 5040	4-h	(Birch and Cary, 1996)
$PM_{2.5}$	The beta-ray method	1-h	(Shin et al., 2011; Takahashi et al., 2008)
O_3	Ozone Analyzer 49iQ	1-min	(Thermo Fisher Scientific, USA)
SO_2	Pulsed Fluorescence SO_2	1-min	(Thermo Fisher Scientific, USA)
CO	Gas Filter Correlation CO Analyzer 48i	1-min	(Thermo Fisher Scientific, USA)
NO	chemiluminescence with a molybdenum converter,	1-min	(Marley et al., 2004)
NO_2	Cavity Attenuated Phase Shift (CAPS) Trace-level NO_2 Analyzer	1-min	(Marley et al., 2004)
β, depolarization ratio	The elastic lidar	15-min, 6 m	(Kim et al., 2007; Kim et al., 2015)

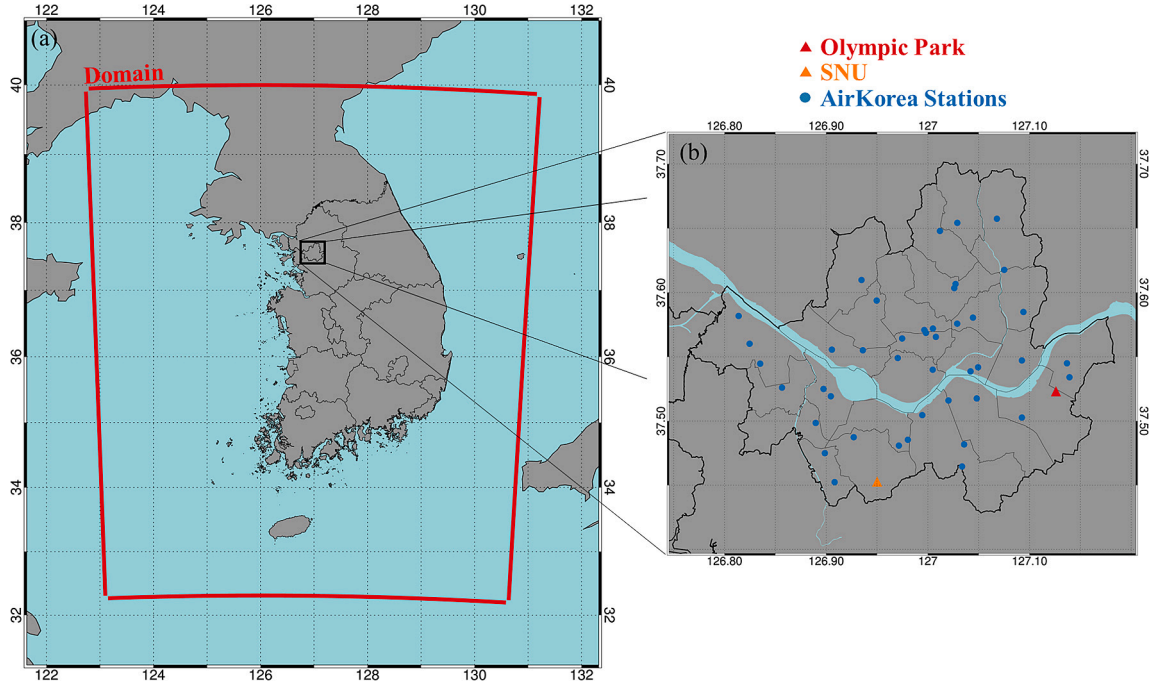

Fig. 1. Map of the model domain and the locations of the Olympic Park site (127.13°E, 37.52°N), the SNU site (126.95°E, 37.45°N), and the AirKorea sites.

Asymmetrical Convective Model v2 (ACM2) schemes (Lee et al., 2023; Mantovani Júnior et al., 2023). Our parameterization addresses this issue based on the systematic evaluation of simulated PBLH and thermodynamic variables against the available observations during the SIJAQ 2021 campaign over the Korean peninsula.

3.2. A new MLH parameterization

Here, we introduce a new parameterization of MLH to detect an upper limit of the thermally/mechanically-induced vertical mixing and replace PBLH in CTMs. We find new criteria to determine MLH based on the detailed analysis of vertical structures and evolutions of related variables such as buoyancy (B), wind shear (W_s), local Richardson number (R_i) (Woods, 1969), and θ_v during the SIJAQ 2021 campaign. B and W_s are expressed as follows:

$$B(z) = \frac{g}{\theta_v}\frac{\partial \theta_v}{\partial z} \tag{4}$$

$$W_s(z) = \sqrt{\left(\frac{\partial u}{dz}\right)^2 + \left(\frac{\partial v}{dz}\right)^2} \tag{5}$$

R_i is the ratio of the buoyancy to the flow shear, expressed as:

$$R_i(z) = \frac{B(z)}{W_s(z)^2} \tag{6}$$

For the MLH parameterization, we use $d\theta_v/dz$. and R_i to account for mechanical and thermal-induced mixing. At each model level, locally computed B, W_s, and R_i are examined to determine MLH. We differentiate ways to determine MLH for day and night conditions.

For the night condition, we use θ_v, a conservative quantity in the mixed layer, to find the top of the mixed layer. Then, we compare the R_i value at the top with the lower levels to check whether mechanical mixing can occur based on stability. Based on this concept and through many sensitivity tests, we set criteria to detect the MLH: the altitude below which θ_v is uniform ($|d\theta_v/dz.| < 0.0075$ K m^{-1}) and R_i begins to increase. For safety purposes, the nighttime upper limit of MLH is set to the nighttime maximum value of observation (800 m) during the campaign. The lower limit of MLH is also set to PBLH from the YSU PBL scheme.

For the daytime condition, we extend MLH to the top of the entrainment zone, where vertical mixing above the PBLH occurs due to countergradients. In the case of the YSU PBL scheme, the top of the entrainment zone is determined based on an arbitrary criterion ε that is a ratio of the entrainment zone to the depth of the vertical layers of the model. However, this criterion does not work effectively due to the coarse resolution of the vertical grids of the model (~120 m at the first model grid and more coarse at the above grids) unless the vertical resolution gets finer to ~20 m. Thus, we increase the criterion value of ε from 4.6 to 50, considering the interval between the vertical grids of the model, based on a discussion with the developer of the YSU PBL scheme (Hong, 2010; Hong et al., 2006).

Fig. 2 shows simulated vertical profiles of θ_v, R_i, and their vertical gradients on October 26, 2021, at 22KST during the campaign. The observed and simulated PBLH and MLH are also shown in the figure. The new parameterization appears to capture discontinuity at ~700 m well, where both θ_v and R_i start to increase. The determined MLH agrees well with the observed PBLH, whereas the simulated PBLH was significantly low.

Fig. 3 presents campaign mean diurnal variations of observed and simulated PBLH and MLH along with hourly columns of simulated B, W_s^2, R_i, and $d\theta_v/dz$. The observed PBLH sustains ~0.5 km at night and grows up to ~1.5 km during the day. The YSU PBL scheme simulates PBLH lower than the observations. The discrepancy in the model is especially significant during the night. This nocturnal underestimation is likely because the YSU PBL scheme diagnoses PBLH based on the averaged bulk Richardson number from the surface to PBLH. This mean quantity likely underestimates local vertical motion caused by mechanical wind shear (S. Hong, personal communication, May 2022).

The MLH parameterization, on the other hand, is based on the local Richardson number, which enables us to consider local stability at each level. The simulated MLH appears to capture the observed PBLH well. The improvement is pronounced at night when non-negligible W_s, relatively weak B, and a decrease in R_i near 0.5 km occur, indicating vertical mixing by mechanical forcing.

Although our new parameterization captures the observation well compared to the conventional YSU scheme, we acknowledge that our evaluation is relatively limited to the SIJAQ campaign period in the Korean peninsula. More extensive evaluation of the parameterization by comparing against observations, including radiosonde data, should be

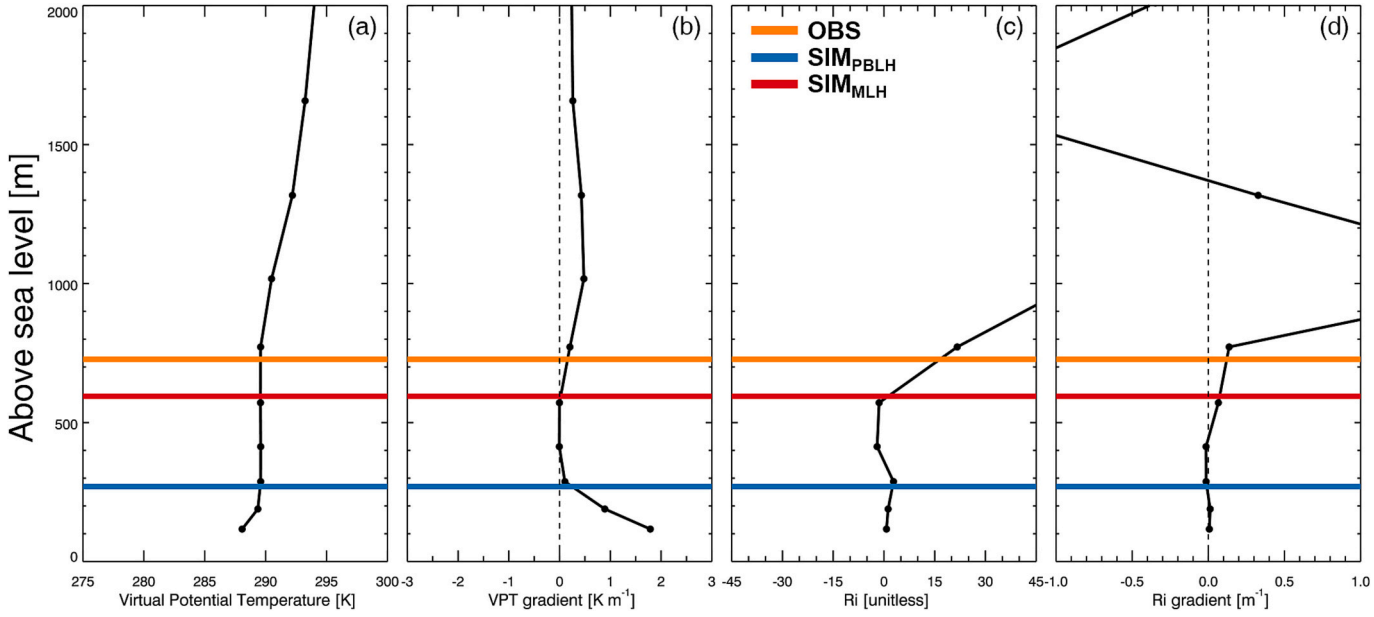

Fig. 2. An example case of MLH determination, presenting simulated vertical profiles of (a) θ_v, (b) $d\theta_v/dz.$, (c) R_i, and $dR_i/dz.$ on October 26, 2021, at 22KST. Each colored solid line indicates observed PBLH (yellow), simulated PBLH (blue), and simulated MLH (red).

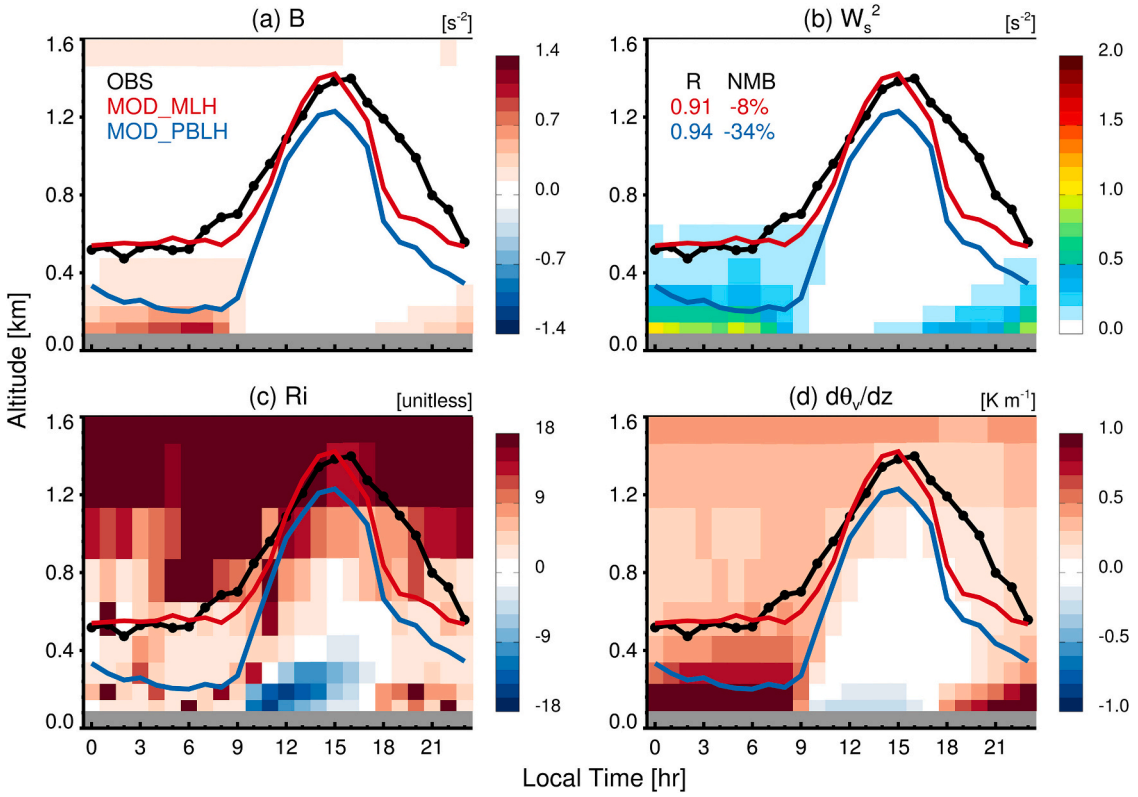

Fig. 3. Averaged diurnal variations of observed PBLH (black), simulated PBLH (blue) from the YSU PBL scheme, and simulated MLH (red). Color-shaded areas indicate hourly varying columns of (a) B, (b) W_s^2, (c) R_i, and (d) $d\theta_v/dz$. from model simulations during the SIJAQ2021 campaign at the SNU.

necessary for different times and areas.

3.3. WRF-GC

We used the WRF-GC version 1.0, an online coupling of the Weather Research and Forecasting (WRF) mesoscale meteorological model (WRF v3.9.1.1) and the GEOS-Chem chemistry model v12.2.1 (Lin et al., 2020). The WRF model provides meteorological variables to drive GEOS-Chem simulations of gas and aerosol species in the atmosphere. More details about the WRF-GC can be found in Lin et al. (2020).

Fig. 1a shows a model domain to cover South Korea (122.7–131.2°E, 32.2–40.0°N) with 9 km × 9 km resolutions and 50 hybrid-sigma vertical layers (up to 10 hPa). We used the final operation global analysis data from the Global Forecasting System of National Centers for Environment Prediction (NCEP-FNL) for meteorological initial and boundary conditions every 6-h.

Table 2 summarizes physical schemes used in WRF simulations. The Rapid Radiative Transfer Model for General Circulation Models (RRTMG) computed short/longwave radiative transfer calculations in the atmosphere (Clough et al., 2005). The Unified Noah land-surface model calculated various processes between the land-surface and the atmosphere in the model (Ek et al., 2003). Grid and subgrid-scale clouds were simulated using the WRF Single Moment 5-class (WSM5) (Hong et al., 2004) and the newer Tiedtke scheme (Hamilton et al., 2011; Tiedtke, 1989). A single-layer urban canopy model (Kusaka and Kimura, 2004) was adopted to simulate urban processes, including building-induced turbulences and the heat island effect. The electronic architectural administration information system (EAIS) of the Ministry of Land, Infrastructure, and Transport of Korea provides statistics for buildings as an input for the urban canopy model (https://www.eais.go.kr/moct/awp/aec02/AWPAEC02L01, accessed September 2, 2024). The YSU PBL scheme (Hong et al., 2006) calculated PBLH and variables related to turbulences in PBL. Furthermore, we adopted a new MLH parameterization in the model and conducted several sensitivity studies to understand the effects of mixing on chemistry, especially for nighttime. One thing to note is that MLH was calculated in WRF but only used for the vertical mixing processes of chemistry simulations to evaluate the impacts of MLH on chemistry simulations.

Table 2
Summary of physical schemes used in this study.

Physical process	Option	References
Horizontal grid	78 cells × 93 cells (△X = 9 km)	
Vertical Layer	50 layers (up to 10 hPa)	
Short/Long wave radiation	The Rapid Radiative Transfer Model for General Circulation Models (RRTMG)	(Clough et al., 2005)
Land-surface exchange	The Unified Noah land-surface model	(Ek et al., 2003)
Grid-scale cloud	The WRF Single Moment 5-class (WSM5)	(Hong et al., 2004)
Subgrid-scale cloud	New Tiedtke scheme	(Hamilton et al., 2011; Tiedtke, 1989)
Urban processes	A single-layer urban canopy model	(Kusaka and Kimura, 2004)
Turbulence	The YSU PBL scheme	(Hong et al., 2006)
Meteorological initial/ boundary conditions	NCEP FNL (0.5° × 0.5°)	

The WRF-GC computes coupled O_X-NO_X-VOC-halogen-aerosol chemistry in the troposphere (Bey et al., 2001) using unified tropospheric-stratospheric chemistry extension (UCX) (Eastham et al., 2014). The heterogeneous reaction of N_2O_5, a primary source of nighttime HNO_3 and NO_3^-, is simulated based on the method by Bertram and Thornton (2009), considering an organic coating effect on the N_2O_5 uptake (McDuffie et al., 2019) in the model. A thermodynamic equilibrium between gaseous and aerosol species is calculated using an aerosol thermodynamic model, ISORROPIA II (Fountoukis and Nenes,

2007). The simple secondary organic aerosol (SOA) scheme is used to simulate a single lumped SOA precursor that is irreversibly converted to a single lumped SOA tracer (SOAS) with a molecular weight of 150 g mol^{-1} (Hayes et al., 2015; Hodzic and Jimenez, 2011; Shrivastava et al., 2017). We used MLH and eddy diffusivity from the new MLH parameterization to simulate the PBL mixing of chemical species in the model.

The model of Emission of Gases and Aerosols from Nature (MEGAN) version 2.1 (Guenther et al., 2012) simulated isoprene, methyl butanol, etc., from biogenic sources based on activity factors, canopy environment, leaf age, and soil moisture. We adopted the SIJAQ v2 emission inventory for anthropogenic emissions over East Asia, developed by Konkuk University. This inventory provides anthropogenic CO, NO_X, SO_2, NH_3, and VOCs emissions for 2019 with the SAPRC-07 chemical mechanism (Carter, 2010). Species in SAPRC-07 were mapped onto the WRF-GC species (Li et al., 2014). The annual total emissions of CO, NO_X, SO_2, NH_3, and VOCs are 0.8, 1.1, 0.3, 0.3, and 1.0 Tg/yr for South Korea, respectively. The chemical boundary conditions were provided every 6-h from the Global/Regional Integrated Model system-Chemistry Climate Model (GRIMs-CCM), developed by coupling the chemistry modules of the GEOS-Chem to the GRIMs general circulation model (Koo et al., 2022; Lee et al., 2022).

We conducted several model simulations with different mixing schemes from 2019.10.17 00UTC to 2019.11.26 00UTC. The simulated PBLH and MLH were validated by comparing them against observed PBLH derived by lidar at SNU. Furthermore, we evaluated the model performances by comparing simulated versus observed gaseous/aerosol concentrations at Olympic Park. For convenience, WRF-GC simulations with PBLH and MLH are hereafter called SIM_{PBLH} and SIM_{MLH}, respectively.

4. Model evaluation

Fig. 4 shows the hourly mean observed versus simulated PBLH and MLH at SNU during the campaign. The observed PBLH shows typical diurnal variations that increase in the daytime and decrease at night. The daytime peak of observed PBLH reaches up to 1900 m, whereas the nighttime PBLH sustains above 400 m. Simulated values also reproduce observed diurnal variations. As mentioned above, however, simulated PBLH shows significant underestimation, especially at night, with a normalized mean bias (NMB) of −49 % compared to the observed values. Our comparison is consistent with previous studies reporting nighttime underestimations of simulated PBLH during the KORUS-AQ campaign (Oak et al., 2019; Travis et al., 2022). On the other hand, the simulated MLH presents a better agreement with the observation than the simulated PBLH, showing −10 % of NMB during the campaign. Especially, the new parameterization well captures nighttime observed PBLH of 400–500 m. The simulated MLH also shows better agreement in reproducing daily peaks of observed PBLH than the simulated PBLH.

Here, we also examined the impact of using the simulated MLH instead of the simulated PBLH on model performances in gaseous and aerosol simulations. Figs. 5 and S1 compare gaseous species concentrations from SIM_{PBLH} and SIM_{MLH} with observations at the Olympic Park site during the campaign. The observed NO and NO_2 concentrations show bimodal increases because of enhancement in mobile emissions in rush hour, reaching up to 200 ppbv and 60 ppbv, respectively. The observed O_3 concentrations typically increase in the daytime and decrease at night. The peak concentration of O_3 reached 75 ppbv during the campaign. The observed CO concentrations also show bimodal increases in rush hour and the ranges of 50–750 ppbv. The observed SO_2 and NH_3 concentrations vary with the ranges of 1.5–4 ppbv and 2–13 ppbv but do not present distinct diurnal variations.

The simulated gaseous species from SIM_{PBLH} and SIM_{MLH} generally reproduce the observed day-to-day variations of NO_2, O_3, and CO, showing moderate correlation coefficients (R) over 0.4. However, for NO, SO_2, and NH_3, both SIM_{PBLH} and SIM_{MLH} show poor correlation coefficients smaller than 0.3. These poor correlations can be attributed to the representation issue of the Olympic Park site in the model. The site is located in the middle of a green space surrounded by a high-density residential area and freeways in the SMA, which cannot be resolved due to the coarse spatial resolution of the model. SIM_{MLH} is slightly less correlated with the observations than SIM_{PBLH}, except for NO during the campaign, but the difference between the two models is insignificant. However, we find that campaign-averaged diurnal variations were well captured by SIM_{MLH} with higher R values than SIM_{PBLH}, except for NO_2, as shown in Fig. S1.

The difference between SIM_{PBLH} and SIM_{MLH} stands out at night. The

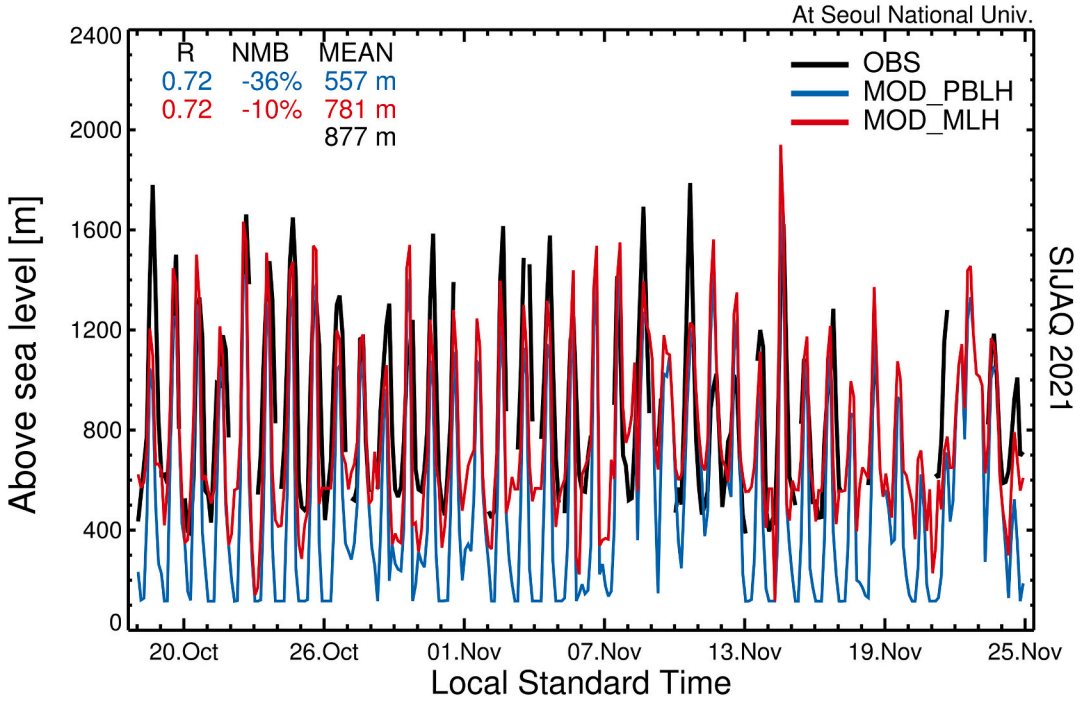

Fig. 4. Hourly time series of the observed PBLH (black) and simulated PBLH (blue) and MLH (red) during the SIJAQ 2021 campaign.

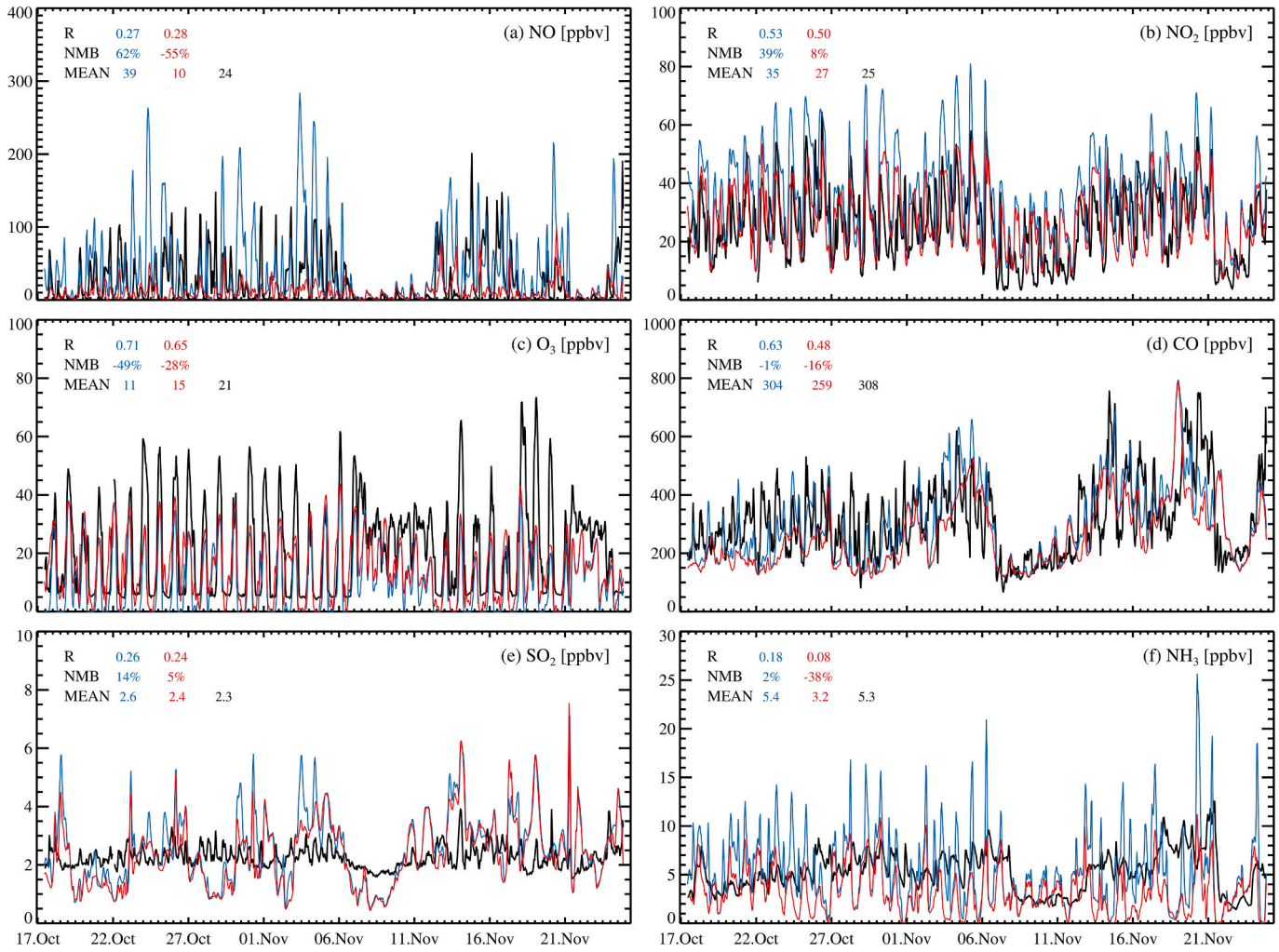

Fig. 5. Hourly time series of the observed (black) and simulated gaseous species from SIM_{PBLH} (blue) and SIM_{MLH} (red), including (a) NO, (b) NO_2, (c) O_3, (d) CO, (e) SO_2, and (f) NH_3 at the Olympic Park site during the SIJAQ 2021 campaign.

nighttime underestimation of PBLH in SIM_{PBLH} leads to the accumulation of surface-emitted NO and NO_2 near the surface and its significant overestimation with 62 % and 39 % of NMB, respectively. However, extended mixing volume in SIM_{MLH} alleviates this overestimation in NO to −55 % and in NO_2 to 8 % of NMB. The nighttime NO overestimation in SIM_{PBLH} also triggers too fast titration of O_3 and significant underestimation in O_3 with −49 % NMB. On the other hand, SIM_{MLH} shows some improvement in the nighttime NO-O_3 titration problem of SIM_{PBLH}, reducing the NMB of O_3 to −28 %.

Simulated CO and SO_2 in SIM_{MLH} are slightly lower than in SIM_{PBLH} due to faster ventilation by the extended MLH. Regarding biases in the model, SO2 gets better, but CO worsens in SIM_{MLH}. CO underestimation is attributed to significant uncertainties in the CO emission inventory in East Asia (Park et al., 2021b). Unlike other species, SIM_{PBLH} and SIM_{MLH} fail to capture observed variation and concentrations of NH_3. It is likely related to not only uncertainty in the diurnal variation of NH_3 emissions (Jeppsson, 2002; Lonsdale et al., 2017) but also significant uncertainties in measuring NH_3 concentrations due to its high reactivity, water solubility, and low concentrations (Schobesberger et al., 2023; Sutton et al., 2008).

In Figs. 6 and S2, simulated aerosol species from SIM_{PBLH} and SIM_{MLH} are compared with observations at the Olympic Park site during the campaign. The daily observed SO_4^{2-}, NO_3^-, and NH_4^+ vary consistently, showing almost zero concentrations under conditions favorable to ventilation in P3 but showing peaks of 15 μg m^{-3} in SO_4^{2-}, 65 μg m^{-3} in NO_3^-, and 20 μg m^{-3} in NH_4^+ in P4. The observed BC and OC also vary similarly to SO_4^{2-}, NO_3^-, and NH_4^+, with daily ranges of 0–3 μg m^{-3} in BC and 1–21 μg m^{-3} in OC, respectively. The observed $PM_{2.5}$ concentrations vary in the range of 5–150 μg m^{-3}, contributed mainly by NO_3^-, NH_4^+, and OC. The diurnal variations of aerosol species are shown in Fig. S2. Although the 4-hour time resolutions of the aerosol measurements make it difficult to recognize diurnal variations of the species, SIM_{MLH} shows better NMBs than SIM_{PBLH}, except for OC.

The impacts of using MLH on aerosol species are also evaluated by comparing SIM_{PBLH} and SIM_{MLH}. Underestimated PBLH causes the accumulation of surface-emitted pollutants near the surface. This aspect is manifested in primary aerosol species, such as BC, which is prone to vertical mixing within the boundary layer. Secondary aerosol concentrations, including NO_3^- and NH_4^+, also decrease when using MLH but appear to be buffered by their production processes, such as heterogeneous reactions and thermodynamic partitioning. Interestingly, SO_4^{2-} is not sensitive to variation in boundary layer height, showing almost no changes in correlation coefficients and NMBs in SIM_{PBLH} and SIM_{MLH}. This is likely because SO_4^{2-} is mainly produced by the reaction of SO_2 and OH during the daytime and by the aqueous phase oxidation within clouds. Thus, SO_4^{2-} is likely well distributed below PBLH/MLH and less sensitive to changes in PBLH and MLH at night.

In the cases of NO_3^- and NH_4^+, the extended volume in SIM_{MLH} relative to SIM_{PBLH} notably decreases their concentrations, resulting in better model performances with decreased NMBs from 126 % to 91 % for

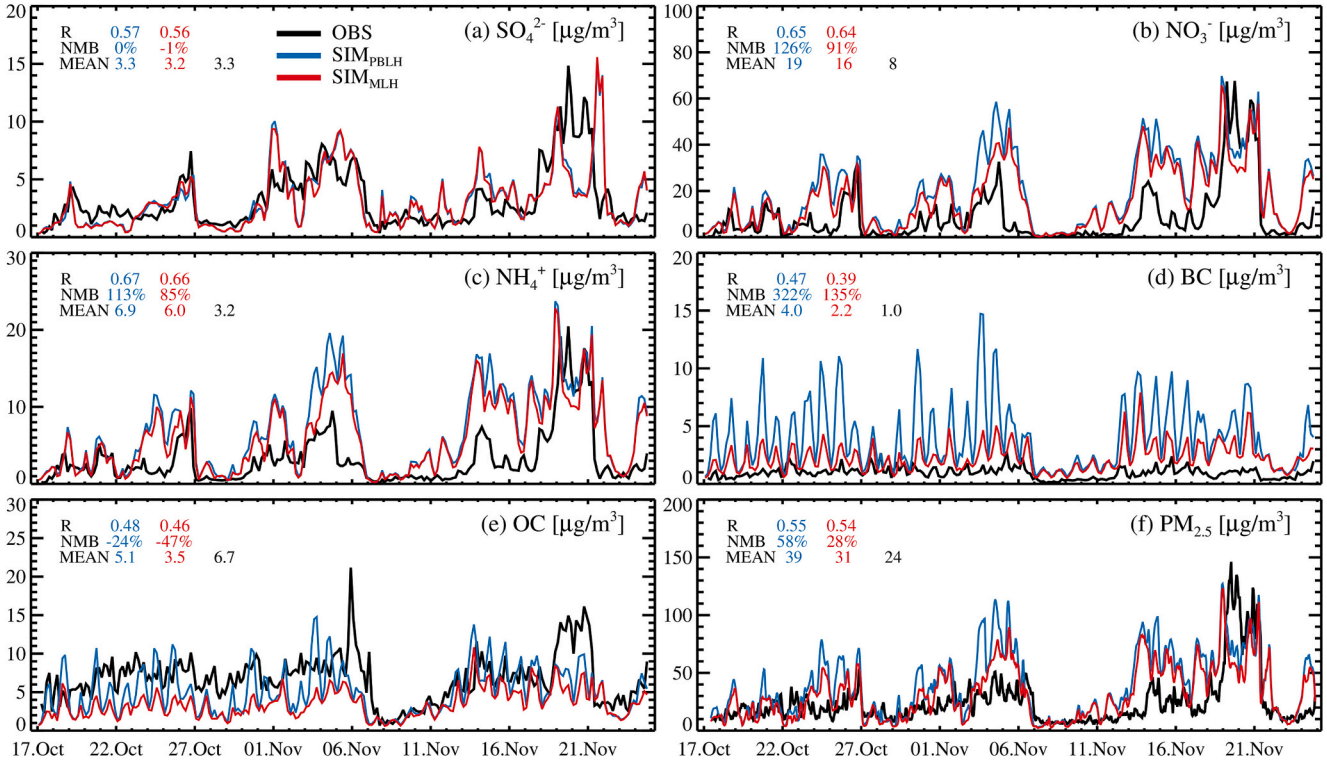

Fig. 6. 4-hourly time series of the observed (black) and simulated aerosol species from SIM_{PBLH} (blue) and SIM_{MLH} (red), including (a) SO_4^{2-}, (b) NO_3^-, (c) NH_4^+, (d) BC, (e) OC, and (f) $PM_{2.5}$ at the Olympic Park site during the SIJAQ 2021 campaign.

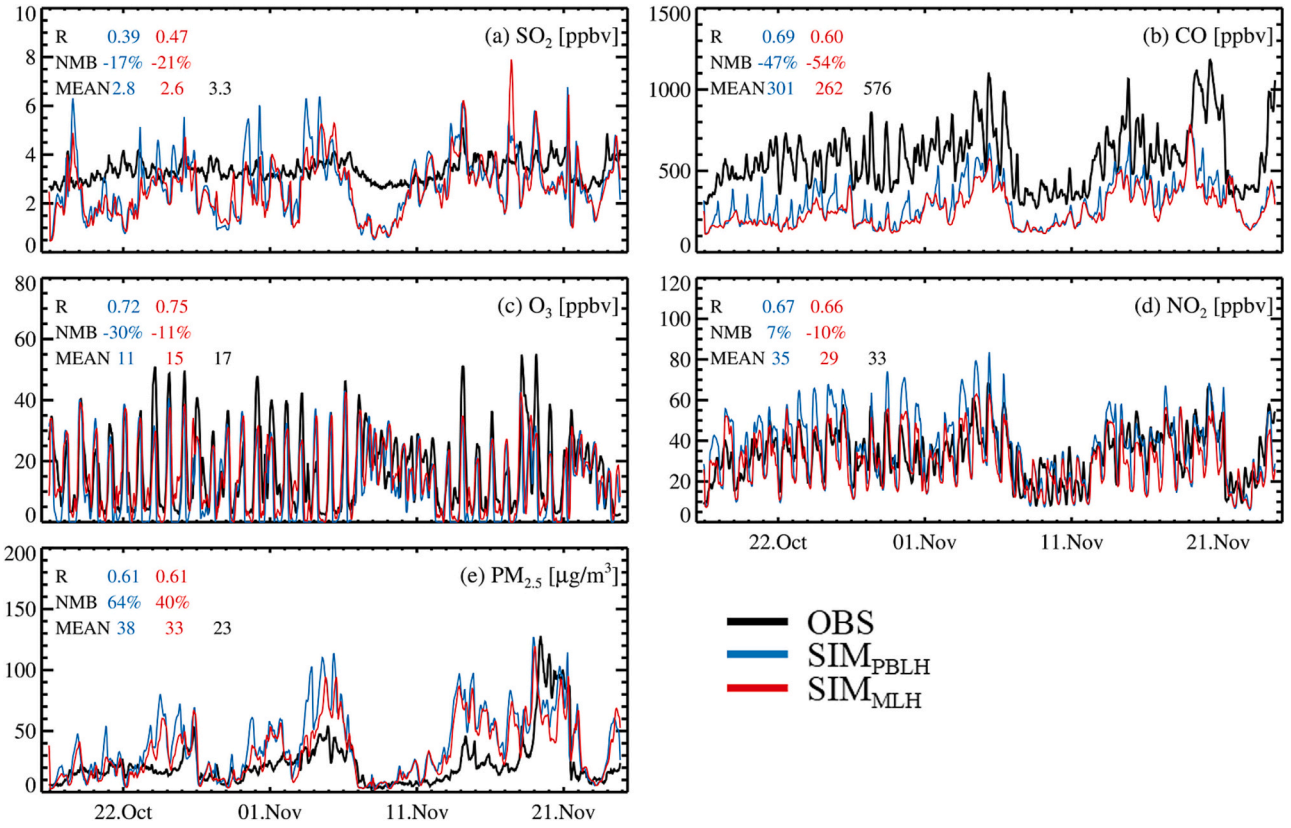

Fig. 7. The hourly time series of the observed (black) and simulated species from SIM_{PBLH} (blue) and SIM_{MLH} (red), including (a) SO_2, (b) CO, (c) O_3, (d) NO_2, and (e) $PM_{2.5}$ averaged over AirKorea sites in Seoul.

NO_3^- and 113 % to 85 % for NH_4^+ without noticeable decreases in correlation coefficients. However, overestimations in the model still exist and are likely related to insufficient dry deposition of HNO_3 (Travis et al., 2022) and the missing uptake of HNO_3 to coarse particulate matter (Zhai et al., 2023).

We also found that conspicuous overestimation in BC concentrations is alleviated from 322 % to 135 %. However, the underestimation of OC gets worse in SIM_{MLH}, but the secondary organic carbon scheme we used here has significant uncertainties (Brewer et al., 2023; Oak et al., 2022), necessitating further research on organic aerosol chemistry. Finally, SIM_{MLH} shows a better agreement in reproducing observed $PM_{2.5}$ concentrations than SIM_{PBLH}, with decreased NMBs from 58 % to 28 %.

We further validated the MLH parameterization by using observations from the AirKorea network. Figs. 7 and S3 compare the observed and simulated species concentrations from SIM_{PBLH} and SIM_{MLH} over Seoul. The observed species show increased concentrations of SO_2, CO, NO_2, and $PM_{2.5}$ in P2 and P4, which is consistent with the observation at the Olympic park (Fig. 5). The peaks in observed CO and $PM_{2.5}$ concentrations are up to 1200 ppbv and 130 μg m^{-3}, respectively.

The simulated CO, O_3, NO_2, and $PM_{2.5}$ concentrations from SIM_{PBLH} and SIM_{MLH} moderately reproduce the observed day-to-day variations with R values over 0.6. We find that the models better capture the observations in a broader region because of the better spatial representation in the models. The impacts of using MLH on the model performance in gaseous and aerosol simulations are consistent with the results at the Olympic park site (Figs. 5 and 6). Underestimation in O_3 and overestimation in $PM_{2.5}$ in the model are improved in SIM_{MLH}. Fig. S3 presents diurnal variations of the observed and simulated species. The tendencies of over/underestimation of species are the same as in Fig. 7. SIM_{MLH} reproduces the diurnal variation better by showing higher R values than SIM_{PBLH}.

In summary, the new MLH improves the excessive accumulation of surface-emitted species near the surface and subsequent problems. In particular, the nighttime NO_X-O_3 problem is alleviated by suppressing too much titration of O_3 by overestimated NO_X. The NMB of $PM_{2.5}$ also decreases due to the improvement in NO_3^-, NH_4^+, and BC overestimations. Although aerosol concentrations in SIM_{MLH} are slightly less correlated with the observations compared to SIM_{PBLH}, as shown in Fig. 5, differences are insignificant compared to gaseous species, likely due to the buffered impacts of aerosol production processes. Thus, we conclude that using MLH in the model instead of PBLH improves the model's performance.

5. Impacts of MLH on nighttime chemistry

This section examines how active vertical mixing by PBL correction alters nighttime chemistry simulations. Fig. 8 presents nighttime differences between SIM_{PBLH} and SIM_{MLH}, including aerosol surface areas, N_2O_5, and TNO_3 (HNO_3 + NO_3^-) at the surface during the campaign. N_2O_5 is one of the nighttime reservoirs of NO_X and undergoes heterogeneous reactions on the aerosol surface, producing HNO_3 (Jacob, 2000). Our PBL correction induces more active vertical mixing of aerosols within the boundary layer and causes a decrease in aerosol surface area in the surface air, consequently slowing down the rate of the N_2O_5 heterogeneous reaction. Because the heterogeneous reaction of N_2O_5 is the primary process of nighttime TNO_3 production, the concentrations of TNO_3 also decrease, along with more dilution of the surface TNO_3 by the PBL correction. Also, more lofted pollutants are likely transported further by stronger wind above the surface, showing the pronounced impacts of PBL correction in the downwind regions of the significant sources. As a result of PBL correction, aerosol surface area and TNO_3 concentration are reduced by up to 10 %, but N_2O_5 concentrations increase by up to 80 %.

Our PBL correction also alters the thermodynamic equilibrium between HNO_3 and NO_3^-. Fig. 9 shows the impacts of PBL correction on vertical distributions of the species (N_2O_5, HNO_3, NH_3, and NO_3^-) related

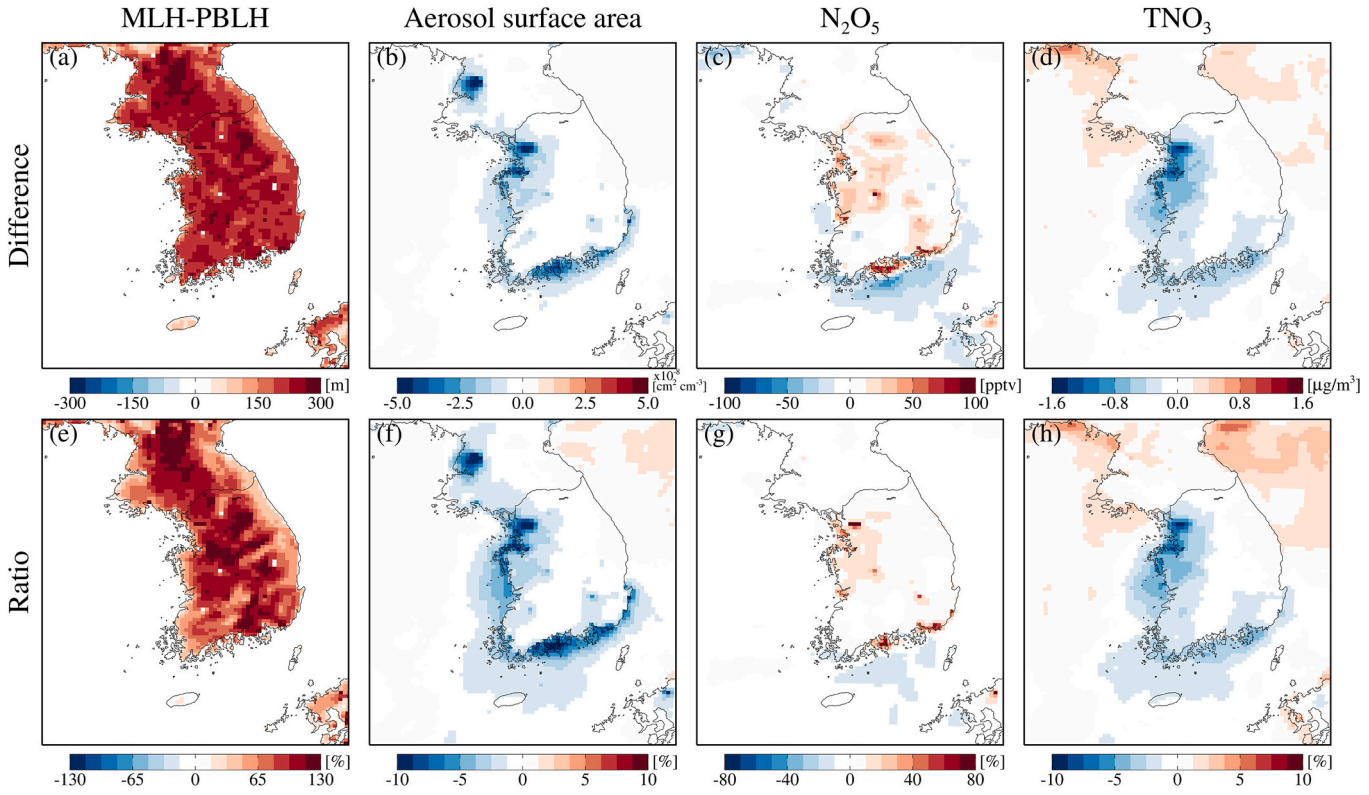

Fig. 8. Averaged Spatial distributions of differences (SIM_{MLH}-SIM_{PBLH}) in (a) boundary layer height, (b) aerosol surface area, (c) N_2O_5, and (d) TNO_3 (HNO_3 + NO_3^-) at the surface during the SIJAQ campaign, indicating the impacts of our new parameterization on the model simulations, particularly for nighttime. The ratios of the impacts (e–h) are calculated by (SIM_{MLH}-SIM_{PBLH})/SIM_{PBLH} × 100.

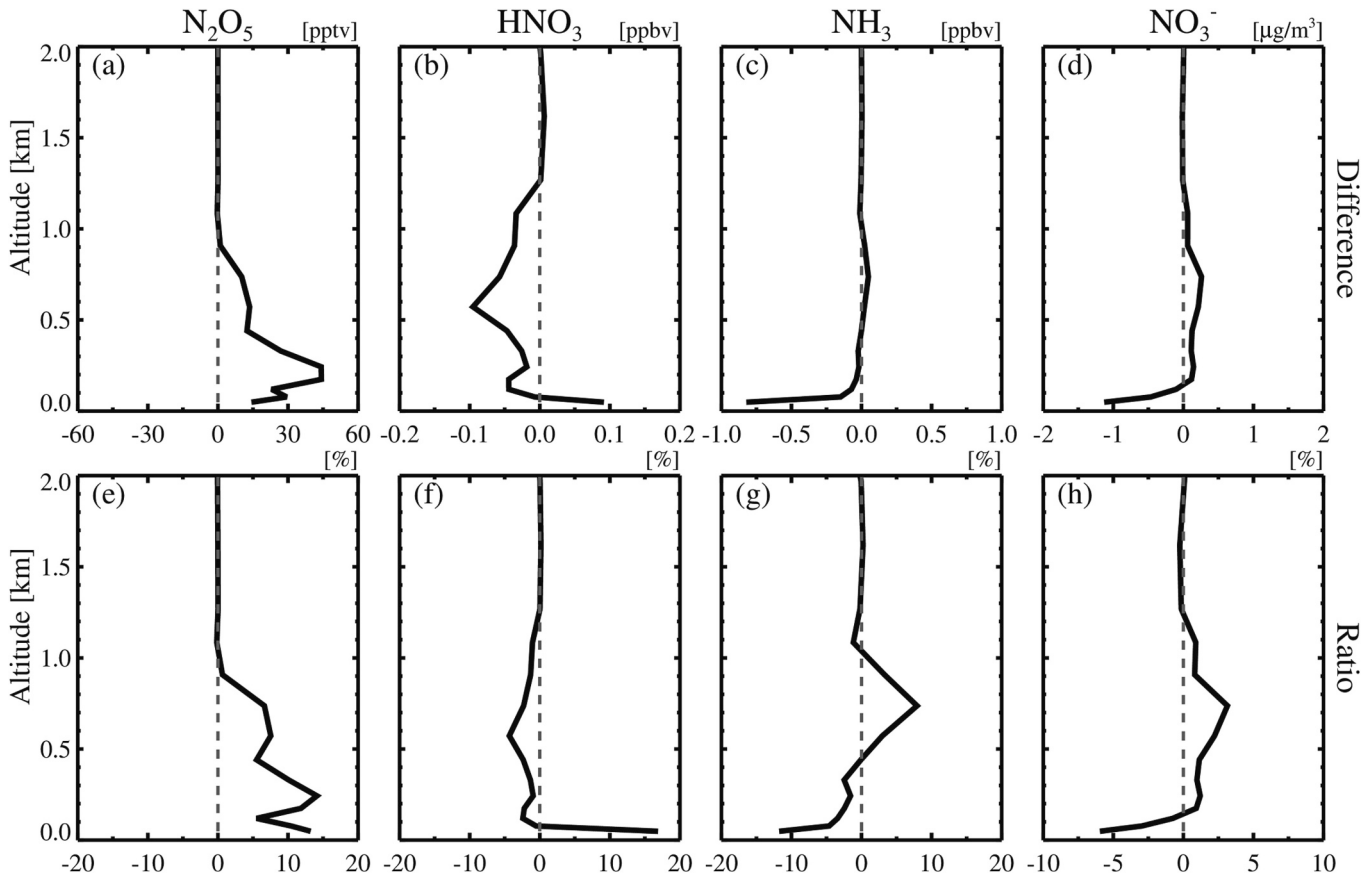

Fig. 9. Campaign-mean vertical distributions of the impacts of PBL correction (SIM_{MLH}-SIM_{PBLH}) on (a) N_2O_5, (b) HNO_3, (c) NH_3, and (d) NO_3^- over SMA during the SIJAQ campaign. The ratios of the impacts (e-f) are calculated by (SIM_{MLH}-SIM_{PBLH})/SIM_{PBLH} × 100.

to nighttime NO_X chemistry. As discussed above, PBL correction slows down the heterogeneous reaction of N_2O_5, as indicated by N_2O_5 increases and TNO_3 decreases, respectively. Furthermore, PBL correction leads to the dilution of surface-emitted NH_3 and less NO_3^- production under NH_3-limited conditions near the surface. This change again affects the reduction in aerosol surface area and TNO_3 production, resulting in a nonlinear feedback between aerosol and N_2O_5 heterogeneous reactions.

6. Summary and discussions

We introduce a novel parameterization for the mixed layer height (MLH) based on the Yonsei University (YSU) planetary boundary layer (PBL) scheme. The MLH parameterization is designed to find the top of vertical mixing in the boundary layer using R_i and $d\theta_v/dz$., accounting for thermal and mechanical mixing. The parameterization shows better agreement with the observed PBLH, particularly addressing the underestimation issue of PBLH at night in the model.

The MLH parameterization was further validated by comparing the model performances of SIM_{PBLH} and SIM_{MLH} in gaseous and aerosol simulations during the SIJAQ campaign. PBL correction improves the excessive accumulation of surface-emitted pollutants, resulting in improved agreement with the observed concentrations with reduced NMBs of NO_X (50 % to −27 %) and O_3 (−49 % to −28 %). This approach also improves aerosol simulation, particularly for NO_3^-, NH_4^+, BC, and $PM_{2.5}$, compared with the model using the conventional PBL scheme.

The model results reveal that PBL correction significantly impacts nighttime NO_X chemistry. The enhanced vertical mixing by PBL correction reduces aerosol surface area, decelerating the N_2O_5 heterogeneous reaction while reducing TNO_3 concentrations by up to 10 %. Intriguingly, N_2O_5 concentrations increase by up to 80 %, indicating its sensitivity to PBL correction. Furthermore, PBL correction affects the thermodynamic equilibrium between HNO_3 and NO_3^-, which is associated with vertical distributions of NH_3 concentration in the boundary layer. Our findings in this study imply the intricate interplay between aerosols, NO_X chemistry, and boundary layer mixing, which can play an essential role in determining urban air quality.

CRediT authorship contribution statement

Hyeonmin Kim: Writing – original draft, Visualization, Software, Methodology, Formal analysis, Data curation, Conceptualization. **Rokjin J. Park:** Writing – review & editing, Supervision, Resources, Methodology, Funding acquisition, Conceptualization. **Song-you Hong:** Writing – review & editing, Methodology, Conceptualization. **Do-Hyeon Park:** Writing – review & editing, Data curation. **Sang-Woo Kim:** Writing – review & editing, Data curation. **Yujin J. Oak:** Writing – review & editing, Conceptualization. **Xu Feng:** Methodology. **Haipeng Lin:** Writing – review & editing, Methodology. **Tzung-May Fu:** Methodology.

Funding

This work was supported by Korea Environment Industry &Technology Institute (KEITI) through "Climate Change R&D Project for New Climate Regime.", funded by Korea Ministry of Environment (MOE) (2022003560004). This work was supported by the National Research Foundation of Korea (NRF) grant funded by the Korea government (MSIT) (No. 2018R1A5A1024958).

Declaration of competing interest

The authors declare that they have no known competing financial

interests or personal relationships that could have appeared to influence the work reported in this paper.

Acknowledgments

We thank all participants of the SIJAQ team for their dedication during the field campaign and the agencies operating the measurements at ground sites.

Appendix A. Supplementary data

Supplementary data to this article can be found online at https://doi.org/10.1016/j.scitotenv.2024.176838.

Data availability

The SIJAQ observational dataset used in this study can be obtained by request through the data archive website (https://www.sijaq.org/home, accessed September 2, 2024).

WRF-GC can be downloaded from https://github.com/jimmielin/wrf-gc-release (accessed September 2, 2024).

The WRF-GC model with the MLH parameterization in this study can be made available upon request.

References

Banks, R.F., Baldasano, J.M., 2016. Impact of WRF model PBL schemes on air quality simulations over Catalonia. Spain. Science of The Total Environment 572, 98–113.

Bertram, T.H., Thornton, J.A., 2009. Toward a general parameterization of N_2O_5 reactivity on aqueous particles: the competing effects of particle liquid water, nitrate and chloride. Atmos. Chem. Phys. 9, 8351–8363. https://doi.org/10.5194/acp-9-8351-2009.

Bey, I., Jacob, D.J., Yantosca, R.M., Logan, J.A., Field, B.D., Fiore, A.M., et al., 2001. Global modeling of tropospheric chemistry with assimilated meteorology: model description and evaluation. J. Geophys. Res.-Atmos. 106, 23073–23095.

Birch, M.E., Cary, R.A., 1996. Elemental carbon-based method for monitoring occupational exposures to particulate diesel exhaust. Aerosol Sci. Tech. 25, 221–241.

Bravo-Aranda, J.A., de Arruda, Moreira G., Navas-Guzmán, F., Granados-Muñoz, M.J., Guerrero-Rascado, J.L., Pozo-Vázquez, D., et al., 2017. A new methodology for PBL height estimations based on lidar depolarization measurements: analysis and comparison against MWR and WRF model-based results. Atmospheric Chemistry and Physics 17, 6839–6851.

Brewer, J.F., Jacob, D.J., Jathar, S.H., He, Y., Akherati, A., Zhai, S., et al., 2023. A scheme for representing aromatic secondary organic aerosols in chemical transport models: application to source attribution of organic aerosols over South Korea during the KORUS-AQ campaign. J. Geophys. Res. Atmos. 128, e2022JD037257.

Canuto, V.M., Howard, A., Cheng, Y., Dubovikov, MS., 2001. Ocean Turbulence. Part I: one-point closure model—momentum and heat vertical diffusivities. J. Phys. Oceanogr. 31, 1413–1426.

Carter, W.P.L., 2010. Development of the SAPRC-07 chemical mechanism. Atmos. Environ. 44, 5324–5335.

Clough, S.A., Shephard, M.W., Mlawer, E.J., Delamere, J.S., Iacono, M.J., Cady-Pereira, K., et al., 2005. Atmospheric radiative transfer modeling: a summary of the AER codes. J. Quant. Spectrosc. Radiat. Transf. 91, 233–244.

Eastham, S.D., Weisenstein, D.K., Barrett, S.R.H., 2014. Development and evaluation of the unified tropospheric–stratospheric chemistry extension (UCX) for the global chemistry-transport model GEOS-Chem. Atmos. Environ. 89, 52–63.

Ek, M.B., Mitchell, K.E., Lin, Y., Rogers, E., Grunmann, P., Koren, V., et al., 2003. Implementation of Noah land surface model advances in the National Centers for environmental prediction operational mesoscale eta model. J. Geophys. Res. Atmos. 108.

Fountoukis, C., Nenes, A., 2007. ISORROPIA II: a computationally efficient thermodynamic equilibrium model for K+–Ca 2+–Mg 2+–NH 4+–Na+–SO 4 2−–NO 3−–Cl−–H 2 O aerosols. Atmospheric Chemistry and Physics 7, 4639–4659.

Gerbig, C., Körner, S., Lin, J.C., 2008. Vertical mixing in atmospheric tracer transport models: error characterization and propagation. Atmospheric Chemistry and Physics 8, 591–602.

Guenther, A.B., Jiang, X., Heald, C.L., Sakulyanontvittaya, T., Duhl, T., Emmons, L.K., et al., 2012. The model of emissions of gases and aerosols from nature version 2.1 (MEGAN2.1): an extended and updated framework for modeling biogenic emissions. Geosci. Model Dev. 5, 1471–1492.

Hamilton, K., Wang, Y., Zhang, C., 2011. Improved representation of boundary layer clouds over the Southeast Pacific in ARW-WRF using a modified Tiedtke cumulus parameterization scheme*. Mon. Weather Rev. 139, 3489–3513.

Hayes, P.L., Carlton, A.G., Baker, K.R., Ahmadov, R., Washenfelder, R.A., Alvarez, S., et al., 2015. Modeling the formation and aging of secondary organic aerosols in Los Angeles during CalNex 2010. Atmos. Chem. Phys. 15, 5773–5801.

Hodzic, A., Jimenez, J.L., 2011. Modeling anthropogenically controlled secondary organic aerosols in a megacity: a simplified framework for global and climate models. Geosci. Model Dev. 4, 901–917.

Holtslag, A.A.M., Boville, B.A., 1993. Local versus nonlocal boundary-layer diffusion in a global climate model. J. Climate 6, 1825–1842.

Hong, S.-Y., 2010. A new stable boundary-layer mixing scheme and its impact on the simulated east Asian summer monsoon. Q. J. Roy. Meteorol. Soc. 136, 1481–1496.

Hong, S.-Y., Dudhia, J., Chen, S.-H., 2004. A revised approach to ice microphysical processes for the bulk parameterization of clouds and precipitation. Mon. Weather Rev. 132, 103–120.

Hong, S.-Y., Noh, Y., Dudhia, J., 2006. A new vertical diffusion package with an explicit treatment of entrainment processes. Mon. Weather Rev. 134, 2318–2341.

Jacob, D.J., 2000. Heterogeneous chemistry and tropospheric ozone. Atmos. Environ. 34, 2131–2159.

Jeppsson, K.H., 2002. SE—structures and environment: diurnal variation in Ammonia, carbon dioxide and water vapour emission from an uninsulated, deep litter building for growing/finishing pigs. Biosyst. Eng. 81, 213–223.

Jia, W., Zhang, X., 2020. The role of the planetary boundary layer parameterization schemes on the meteorological and aerosol pollution simulations: a review. Atmos. Res. 239, 104890.

Jordan, N.S., Hoff, R.M., Bacmeister, J.T., 2010. Validation of Goddard earth observing system-version 5 MERRA planetary boundary layer heights using CALIPSO. J. Geophys. Res. Atmos. 115.

Kim, S.-W., Yoon, S.-C., Won, J.-G., Choi, S.-C., 2007. Ground-based remote sensing measurements of aerosol and ozone in an urban area: a case study of mixing height evolution and its effect on ground-level ozone concentrations. Atmos. Environ. 41, 7069–7081.

Kim, M.-H., Yeo, H., Sugimoto, N., Lim, H.-C., Lee, C.-K., Heo, B.-H., et al., 2015. Estimation of particle mass concentration from Lidar measurement. Atmosphere. Korean Meteorological Society 25, 169–177.

Kim, M.-H., Yeo, H., Park, S., Park, D.-H., Omar, A., Nishizawa, T., et al., 2021. Assessing CALIOP-derived planetary boundary layer height using ground-based Lidar. Remote Sens. (Basel) 13, 1496.

Kim, H., Park, R.J., Kim, S., Brune, W.H., Diskin, G.S., Fried, A., et al., 2022. Observed Versus Simulated OH Reactivity during KORUS-AQ Campaign: Implications for Emission Inventory and Chemical Environment in East Asia. Science of the Anthropocene, Elementa, p. 10.

Kim, C.-H., Jo, H.-Y., Jo, Y.-J., Lee, H.-J., Kim, J.-M., Lee, N.-M., et al., 2023. Synoptic meteorological conditions and contributing factors to air quality during the SIJAQ campaign. Atmos. Environ. 309, 119939.

Koo, M.-S., Song, K., Kim, J.-E.E., Son, S.-W., Chang, E.-C., Jeong, J.-H., et al., 2022. The global/regional integrated model system (GRIMs): an update and seasonal evaluation. Asia Pac. J. Atmos. Sci. 59 (2), 113–132. https://doi.org/10.1007/s13143-022-00297-y.

Kusaka, H., Kimura, F., 2004. Coupling a single-layer urban canopy model with a simple atmospheric model: impact on urban Heat Island simulation for an idealized case. Journal of the Meteorological Society of Japan. Ser. II (82), 67–80.

Lee, S., Park, R.J., Hong, S.-Y., Koo, M.-S., Jeong, J.I., Yeh, S.-W., et al., 2022. A new chemistry-climate model GRIMs-CCM: model evaluation of interactive chemistry-meteorology simulations. Asia-Pac. J. Atmos. Sci. 58, 647–666.

Lee, H.-J., Jo, H.-Y., Kim, J.-M., Bak, J., Park, M.-S., Kim, J.-K., et al., 2023. Nocturnal boundary layer height uncertainty in particulate matter simulations during the KORUS-AQ campaign. Remote Sens. (Basel) 15, 300.

Li, M., Zhang, Q., Streets, D.G., He, K.B., Cheng, Y.F., Emmons, L.K., et al., 2014. Mapping Asian anthropogenic emissions of non-methane volatile organic compounds to multiple chemical mechanisms. Atmospheric Chemistry and Physics 14, 5617–5638.

Li, Z., Guo, J., Ding, A., Liao, H., Liu, J., Sun, Y., et al., 2017. Aerosol and boundary-layer interactions and impact on air quality. Natl. Sci. Rev. 4, 810–833.

Li, H., Liu, B., Ma, X., Jin, S., Ma, Y., Zhao, Y., et al., 2021. Evaluation of retrieval methods for planetary boundary layer height based on radiosonde data. Atmos. Meas. Tech. 14, 5977–5986.

Liang, X.-Z., Liu, S., 2010. Observed diurnal cycle climatology of planetary boundary layer height. J. Climate 23, 5790–5809.

Lin, H., Feng, X., Fu, T.-M., Tian, H., Ma, Y., Zhang, L., et al., 2020. WRF-GC (v1.0): online coupling of WRF (v3.9.1.1) and GEOS-Chem (v12.2.1) for regional atmospheric chemistry modeling – part 1: description of the one-way model. Geosci. Model Dev. 13, 3241–3265.

Lonsdale, C.R., Hegarty, J.D., Cady-Pereira, K.E., Alvarado, M.J., Henze, D.K., Turner, M. D., et al., 2017. Modeling the diurnal variability of agricultural ammonia in Bakersfield, California, during the CalNex campaign. Atmos. Chem. Phys. 17, 2721–2739.

Mantovani Júnior, J.A., Aravéquia, J.A., Carneiro, R.G., Fisch, G., 2023. Evaluation of PBL parameterization schemes in WRF model predictions during the dry season of the Central Amazon Basin. Atmosphere 14, 850.

Marley, N.A., Gaffney, J.S., White, R.V., Rodriguez-Cuadra, L., Herndon, S.E., Dunlea, E., et al., 2004. Fast gas chromatography with luminol chemiluminescence detection for the simultaneous determination of nitrogen dioxide and peroxyacetyl nitrate in the atmosphere. Rev. Sci. Instrum. 75, 4595–4605.

McDuffie, E.E., Womack, C.C., Fibiger, D.L., Dube, W.P., Franchin, A., Middlebrook, A. M., et al., 2019. On the contribution of nocturnal heterogeneous reactive nitrogen chemistry to particulate matter formation during wintertime pollution events in northern Utah. Atmos. Chem. Phys. 19, 9287–9308.

Oak, Y.J., Park, R.J., Schroeder, J.R., Crawford, J.H., Blake, D.R., Weinheimer, A.J., et al., 2019. Evaluation of Simulated O3 Production Efficiency during the KORUS-AQ

Campaign: Implications for Anthropogenic NOx Emissions in Korea. Science of the Anthropocene, Elementa, p. 7.
Oak, Y.J., Park, R.J., Jo, D.S., Hodzic, A., Jimenez, J.L., Campuzano-Jost, P., et al., 2022. Evaluation of secondary organic aerosol (SOA) simulations for Seoul, Korea. Journal of Advances in Modeling Earth Systems 14, e2021MS002760.
Onwukwe, C., Jackson, P.L., 2020. Evaluation of CMAQ modeling sensitivity to planetary boundary layer parameterizations for gaseous and particulate pollutants over a fjord valley. Atmos. Environ. 233, 117607.
Pappalardo, G., Amodeo, A., Apituley, A., Comeron, A., Freudenthaler, V., Linné, H., et al., 2014. EARLINET: towards an advanced sustainable European aerosol lidar network. Atmos. Meas. Tech. 7, 2389–2409.
Park, D.-H., Kim, S.-W., Kim, M.-H., Yeo, H., Park, S.S., Nishizawa, T., et al., 2021a. Impacts of local versus long-range transported aerosols on PM10 concentrations in Seoul, Korea: an estimate based on 11-year PM10 and lidar observations. Sci. Total Environ. 750, 141739.
Park, R.J., Oak, Y.J., Emmons, L.K., Kim, C.-H., Pfister, G.G., Carmichael, G.R., et al., 2021b. Multi-Model Intercomparisons of Air Quality Simulations for the KORUS-AQ Campaign. Science of the Anthropocene, Elementa, p. 9.
Park, S., Kim, M.-H., Yeo, H., Shim, K., Lee, H.-J., Kim, C.-H., et al., 2022. Determination of mixing layer height from co-located lidar, ceilometer and wind Doppler lidar measurements: Intercomparison and implications for PM2.5 simulations. Atmospheric. Pollut. Res. 13, 101310.
Rai, D., Pattnaik, S., 2019. Evaluation of WRF planetary boundary layer parameterization schemes for simulation of monsoon depressions over India. Meteorol. Atmos. Phys. 131, 1529–1548.
Schobesberger, S., D'Ambro, E.L., Vettikkat, L., Lee, B.H., Peng, Q., Bell, D.M., et al., 2023. Airborne flux measurements of ammonia over the southern Great Plains using chemical ionization mass spectrometry. Atmos. Meas. Tech. 16, 247–271.
Shi, Y., Hu, F., Xiao, Z., Fan, G., Zhang, Z., 2020. Comparison of four different types of planetary boundary layer heights during a haze episode in Beijing. Sci. Total Environ. 711, 134928.
Shin, H.H., Hong, S.-Y., 2011. Intercomparison of planetary boundary-layer parametrizations in the WRF model for a single day from CASES-99. Bound.-Lay. Meteorol. 139, 261–281.
Shin, S.E., Jung, C.H., Kim, Y.P., 2011. Analysis of the measurement difference for the PM10 concentrations between Beta-ray absorption and gravimetric methods at Gosan. Aerosol Air Qual. Res. 11, 846–853.
Shrivastava, M., Cappa, C.D., Fan, J., Goldstein, A.H., Guenther, A.B., Jimenez, J.L., et al., 2017. Recent advances in understanding secondary organic aerosol: implications for global climate forcing. Rev. Geophys. 55, 509–559.
Stull, R.B., 1988. An Introduction to Boundary Layer Meteorology. Springer, Netherlands.
Sutton, M.A., Erisman, J.W., Dentener, F., Möller, D., 2008. Ammonia in the environment: from ancient times to the present. Environ. Pollut. 156, 583–604.
Takahashi, K., Minoura, H., Sakamoto, K., 2008. Examination of discrepancies between beta-attenuation and gravimetric methods for the monitoring of particulate matter. Atmos. Environ. 42, 5232–5240.
Tiedtke, M., 1989. A comprehensive mass flux scheme for cumulus parameterization in large-scale models. Mon. Weather Rev. 117, 1779–1800.
Travis, K.R., Crawford, J.H., Chen, G., Jordan, C.E., Nault, B.A., Kim, H., et al., 2022. Limitations in representation of physical processes prevent successful simulation of PM_{2.5} during KORUS-AQ. Atmospheric Chemistry and Physics 22, 7933–7958.
Weitkamp, C., 2006. Lidar: Range-Resolved Optical Remote Sensing of the Atmosphere. Springer, New York.
Woods, J.D., 1969. On Richardson's number as a criterion for laminar-turbulent-laminar transition in the ocean and atmosphere. Radio Sci. 4, 1289–1298.
Zhai, S., Jacob, D.J., Pendergrass, D.C., Colombi, N.K., Shah, V., Yang, L.H., et al., 2023. Coarse particulate matter air quality in East Asia: implications for fine particulate nitrate. Atmos. Chem. Phys. 23, 4271–4281.